Exploring optical properties of 2H- and 1T′-$MoTe_2$ single crystals by spectroscopic ellipsometry

Desman Perdamaian Gulo,[1] Nguyen Tuan Hung,[2,3] Raman Sankar,[4] Riichiro Saito,[2] and Hsiang-Lin Liu[1,*]

[1]*Department of Physics, National Taiwan Normal University, Taipei 11677, Taiwan*

[2]*Department of Physics, Tohoku University, Sendai 980-8578, Japan*

[3]*Frontier Research Institute for Interdisciplinary Sciences, Tohoku University, Sendai 980-8578, Japan*

[4]*Institute of Physics, Academia Sinica, Taipei 10617, Taiwan*

(Received 15 October 2022; revised 22 December 2022; accepted 18 January 2023; published 5 April 2023)

Molybdenum ditelluride ($MoTe_2$) has received considerable attention as a two-dimensional material due to its intriguing physical properties and potential for applications in a variety of devices. The optical properties of 2H- and 1T′-$MoTe_2$ single crystals are investigated in this study using spectroscopic ellipsometry over the spectra range 0.73–6.42 eV and at temperatures of 4.2–500 K. According to the optical absorption spectra at 4.2 K, 2H-$MoTe_2$ has an indirect band gap of 1.06 ± 0.01 eV, whereas 1T′-$MoTe_2$ exhibits semimetal behavior. Furthermore, 2H-$MoTe_2$ has three distinct intralayer A_{1s}, A_{2s}, and B_{1s} excitons, and one interlayer A_{IL} exciton at 1.136 ± 0.002, 1.181 ± 0.001, 1.469 ± 0.006, and 1.21 ± 0.01 eV, respectively. The spin-orbit coupling energy of 2H-$MoTe_2$ is 333 meV and is independent of temperature. By contrast, 1T′-$MoTe_2$ has two low-energy optical transitions at 0.78 ± 0.01 and 1.45 ± 0.01 eV, which are redshifted and broadened upon an increase in temperature, indicating the increased electron-phonon interaction. We characterize the optical transitions of both phases of $MoTe_2$ by comparing experimental data with the results of first-principles calculations.

DOI: 10.1103/PhysRevMaterials.7.044001

I. INTRODUCTION

Spectroscopic ellipsometry is an important optical technique used to obtain the complex dielectric function of materials for a wide range of photon energies. Compared with other techniques, such as approaches based on the reflectance contrast or photoluminescence [1], spectroscopic ellipsometry can be employed to directly derive the complex optical constants of materials; these constants are derived from the two independent ellipsometric parameters of Ψ and Δ [2], which are the amplitude ratio and phase difference, respectively, of *p*- and *s*-polarized light upon its reflection by the surface of materials [3]. An advantage of spectroscopic ellipsometry is that the consistency between the real and imaginary parts of the dielectric function can be determined using the Kramers-Kronig transformation. Standard spectroscopic ellipsometry is typically used to characterize isotropic materials, which have the same optical properties for light polarized in any direction. Furthermore, Mueller matrix spectroscopic ellipsometry [4] can determine the different optical properties for different polarization directions in anisotropic materials. Additionally, Mueller matrix spectroscopic ellipsometry can be used to address the linear and circular anisotropic effects in chirality materials. In recent years, spectroscopic ellipsometry has become popular and thus, its importance has been recognized as a method for measuring the optical properties of materials. In this paper, we report the temperature-dependent complex dielectric function for the semiconducting and semimetallic transition-metal dichalcogenides (TMDs) of α-phase $MoTe_2$ (2H-$MoTe_2$) and β-phase $MoTe_2$ (1T′-$MoTe_2$), respectively. Furthermore, we compare the experimental results with first-principles calculations to identify the origin of optical transitions. The present paper aims to obtain the precise optical parameters of 2H-$MoTe_2$ and 1T′-$MoTe_2$ materials as a function of temperature.

TMD materials have recently attracted much attention because of the diversity of their structural phases and potential in practical applications [5,6]. The typical polymorphisms of TMD materials can generally be classified into trigonal prismatic and octahedral structures [7,8]. The 1H, 2H, and 3R phases are characterized by trigonal prismatic structures, whereas the 1T and 1T′ phases are characterized by octahedral structures [9–11]. The structural phases of TMD materials strongly influence their electronic and optical properties. For example, 2H-TMD materials are semiconducting, whereas 1T′-TMD materials exhibit semimetal properties [12]. The optical absorption spectra of 2H-TMD materials contain sharp peaks, whereas the spectra of 1T′-TMD materials are featureless in the infrared to the ultraviolet region [13–15]. Thus, 2H-TMD materials are promising for use as photodetectors, light emitters, and biosensors [16–20]. Furthermore, TMD materials reveal the anisotropic dielectric properties along the in- and out-of-plane directions [21]. The theoretical calculations predict the out-of-plane dielectric constant of the TMD materials increases as the number of layers is increased from monolayer to bulk, whereas the in-plane component remains unchanged [22]. Additionally, because spin-orbit interactions induce small band-gap inversion in metallic TMD materials, 1T′-TMD materials are predicted to have topological properties, and such properties are useful for superconducting and multifunctional-electrode applications [23,24]. Because

*Corresponding author: hliu@ntnu.edu.tw

TMD-based devices have much potential in practical applications, the temperature-dependent complex optical constants must be determined if the effects of self-heating on performance are to be overcome. This study thus investigates the frequency- and temperature-dependent optical properties of 2H- and 1T′-$MoTe_2$ single crystals. The results aid the development of optoelectronic and photonic devices for use over wide photon-energy and temperature ranges.

The $MoTe_2$ material has been of particular interest among TMDs. 2H-$MoTe_2$ is semiconducting and has a hexagonal crystal structure [25]. Bulk 2H-$MoTe_2$ has a smaller indirect band-gap energy of 0.88 eV [26] than other TMD materials [27]. When it is in monolayer form, 2H-$MoTe_2$ has a direct band-gap energy of 1.01 eV [28]. Because of its semiconducting nature, bulk 2H-$MoTe_2$ has highly efficient carrier multiplication [29]. Monolayer 2H-$MoTe_2$ has a relatively large external quantum efficiency (EQE) of 9.5% at 83 K, which is the highest EQE value among monolayer TMDs [30]. Therefore, 2H-$MoTe_2$ has important applications in lasers [31], solar cells [32], and sensors [33]. Conversely, 1T′-$MoTe_2$ is metallic and has a monoclinic crystal structure at room temperature [34]. 1T′-$MoTe_2$ transitions to the orthorhombic γ phase ($1T_d$-$MoTe_2$) at temperatures below 250 K [35]. Bulk 1T′-$MoTe_2$ is metallic and exhibits large magnetoresistance [36]. When it has a thickness of only a few layers, 1T′-$MoTe_2$ exhibits a metal-insulator transition due to strengthening of the carrier localization effect [37]. Hence, 1T′-$MoTe_2$ is promising for applications involving quantum spin Hall insulators [38], topological quantum computation [39], and superconductivity [40]. Our motivation is to investigate both the semiconducting and the semimetallic properties of $MoTe_2$ material from the frequency- and temperature-dependent complex dielectric function.

The optical properties of 2H- and 1T′-$MoTe_2$ single crystals have been investigated at room temperature through spectroscopic ellipsometry over the spectra range 0.59–4.13 eV [41]. Six optical absorption peaks in the spectrum of 2H-$MoTe_2$ are identified as corresponding to A, B, A', B', C, and D excitons. These excitonic transitions occur at the K point (A,B), Γ point (A', B'), and parallel near the Γ point (C,D) in the hexagonal Brillouin zone. The existence of these excitonic features has been confirmed using other techniques, such as reflectance contrast, photoluminescence, photoreflectance, and ultraviolet-visible measurements [1,42,43] and theoretical calculations [44]. By contrast, the optical transitions in 1T′-$MoTe_2$ have not yet been assigned as far as we are aware. The temperature-dependent optical properties of 2H- and 1T′-$MoTe_2$ single crystals have been investigated over a spectral range of 0.5–3.8 eV by using transmission [45,46]. Davey and Evans [45] discovered a small shoulder absorption peak slightly above the location corresponding to the A exciton of 2H-$MoTe_2$ when performing the measurements at 77 K. They assigned this peak to a second transition ($n = 2$) from the A exciton. Furthermore, Beal *et al.* [46] obtained the transmission spectra of 2H- and 1T′-$MoTe_2$ single crystals at temperatures between 5 and 77 K and combined their findings with theoretical calculations. However, the low-frequency optical absorption peaks below 1.0 eV in the spectrum of 1T′-$MoTe_2$ were not assigned. Kimura *et al.* [47] measured the temperature-dependent reflectance spectra of 1T′-$MoTe_2$ single crystals over a spectra range of 8 meV to 1.5 eV. They discovered that 1T′-$MoTe_2$ exhibited type-II Weyl semimetal behavior. More recently, Kopaczek *et al.* [48] explored the optical transitions of 2H-$MoTe_2$ single crystals at temperatures between 20 and 300 K by using reflectance and photoacoustic spectroscopies over a spectra range of 0.8–3 eV. They reported that the band nesting in 2H-$MoTe_2$ was correlated with the strength of electron-phonon coupling.

Most optical measurements of 2H- and 1T′-$MoTe_2$ single crystals have been limited to relatively narrow frequency and temperature ranges. In this paper, we present a comprehensive characterization of the optical properties of 2H- and 1T′-$MoTe_2$ single crystals, and our characterization covers a wide photon-energy range from 0.73 to 6.42 eV and a wide temperature range from 4.2 to 500 K. Results covering a broad frequency range will open new potential applications not only in the near-infrared to visible range, but also in the deep ultraviolet range. In this paper, we report several distinct optical transitions from near infrared to deep ultraviolet at 4.2 K. Furthermore, we perform a band-gap analysis of the optical absorption coefficient to verify that 2H-$MoTe_2$ has an indirect band gap and 1T′-$MoTe_2$ exhibits semimetal behavior. At the lower-energy range, the optical absorption coefficient of 2H-$MoTe_2$ at 4.2 K reveals intralayer A_{1s}, A_{2s}, and B_{1s} excitonic transitions and one interlayer A_{IL} excitonic transition at 1.136 ± 0.002, 1.181 ± 0.001, 1.469 ± 0.006, and 1.21 ± 0.01 eV, respectively. The spin-orbit coupling (SOC) energy of 2H-$MoTe_2$ is found to be 333 meV at all temperatures. By contrast, at 4.2 K, 1T′-$MoTe_2$ exhibits two broad optical absorption bands at 0.78 ± 0.01 and 1.45 ± 0.01 eV. We assign these two optical absorptions to interband transitions between the d orbitals of Mo atoms near the Fermi energy. These two interband absorptions are shifted to lower energy with increasing temperature, indicating the increased electron-phonon interaction.

II. METHODS

A. Experiment

The chemical vapor transport method is used to synthesize 2H- and 1T′-$MoTe_2$ single crystals. Br_2, the source of which is $TeBr_4$, acts as the transport agent and enables effective and rapid vapor transport to produce $MoTe_2$ single crystals. The prereaction temperature of the materials used to grow 2H- and 1T′-$MoTe_2$ single crystals is 800 and 1050° C, respectively. During growth, the temperature is kept at 750 ° C for 2H-$MoTe_2$ and 950 ° C for 1T′-$MoTe_2$. The 2H- and 1T′-$MoTe_2$ single crystals can be grown within 1 week. The procedures used to synthesize the $MoTe_2$ single crystals are identical to those of a previous study [49]. The dimensions of the 2H- and 1T′-$MoTe_2$ single crystals are $0.5 \times 3 \times 6\,mm^3$ and $0.5 \times 10 \times 10\,mm^3$, respectively, as shown in the inset of Supplemental Material Fig. 1 [50]. X-ray powder diffraction is performed at room temperature to determine the quality of the single crystals; the spectra are shown in Supplemental Material Figs. 1(a) and 1(b) [50]. For both single crystals, the platelike pieces are measured in the preferred (00l) orientation [49]. All diffraction peaks of the 2H- and 1T′-$MoTe_2$ single crystals can be indexed, and no impurity is apparent

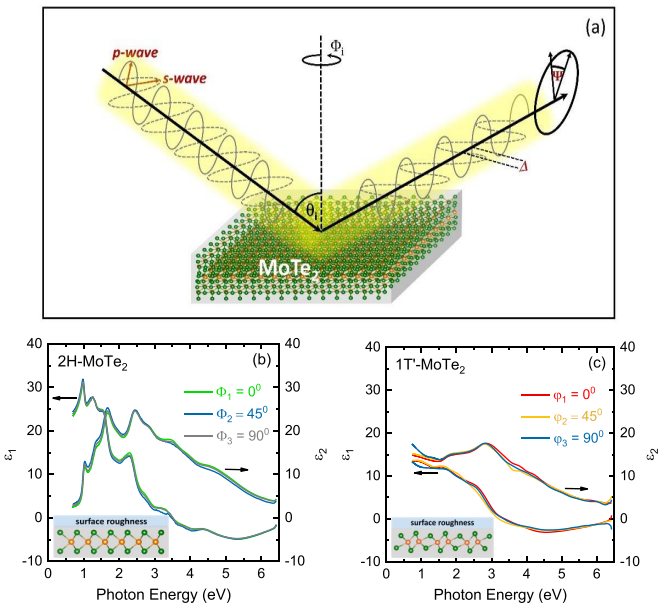

FIG. 1. (a) The schematic of the spectroscopic ellipsometry setup. The real (ε_1) and imaginary (ε_2) parts of the complex dielectric function of (b) 2H- and (c) 1T′-$MoTe_2$ for the sample's azimuthal angle orientation Φ_i of 0°, 45°, and 90°.

above the background level, indicating the high quality of the two samples. The lattice constants of 2H- and 1T′-$MoTe_2$ single crystals were determined in a previous study [49].

We obtain room temperature micro-Raman spectra in the backscattering geometry by using a SENTERRA spectrometer [51]. The laser excitation wavelengths are 488, 532, and 785 nm, respectively. The linearly polarized light is incident on the surface of the 2H- and 1T′-$MoTe_2$ samples and has a diameter spot size of 3 μm. The scattered light is collected using a 1024-pixel-wide charge-coupled detector with a spectral resolution of less than 0.5 cm^{-1}. The laser power is kept at less than 1.0 mW to prevent any heating effects. The Raman spectra of the 2H- and 1T′-$MoTe_2$ single crystals, obtained using 488-, 532-, and 785-nm laser excitation, are presented in Supplemental Material Fig. 2 [50]. The Raman spectra of 2H-$MoTe_2$ show that the E^1_{2g} mode is more prominent under 488- and 532-nm laser excitation, whereas the A_{1g} mode is dominant under 785-nm laser excitation. By contrast, the Raman spectra of 1T′-$MoTe_2$ reveal that the ^3A_g mode is strong for excitation at all wavelengths. Our Raman spectra obtained under laser excitation at 532 nm are consistent with those published previously [52,53].

We measure the optical properties of 2H- and 1T′-$MoTe_2$ single crystals by using an ellipsometer (J. A. Woollam Co.; M-2000U) that covers a spectra range of 0.73–6.42 eV [51]. Figure 1(a) displays the experimental setup used to perform spectroscopic ellipsometry. θ_i is the angle of incidence. We carry out an experiment with multiple incident angles from 55° to 75° to maximize the different reflected light intensities between the p wave and the s wave. Φ_i is the azimuthal orientation on the basal plane of 2H- and 1T′-$MoTe_2$, which is 0°, 45°, or 90°. Spectroscopic ellipsometry measures the change of polarization upon the reflection from the sample surface. The raw ellipsometric data Ψ and Δ are related to the complex Fresnel reflection coefficients as follows [3]:

$$\tan \Psi e^{i\Delta} = \frac{r_p}{r_s}, \tag{1}$$

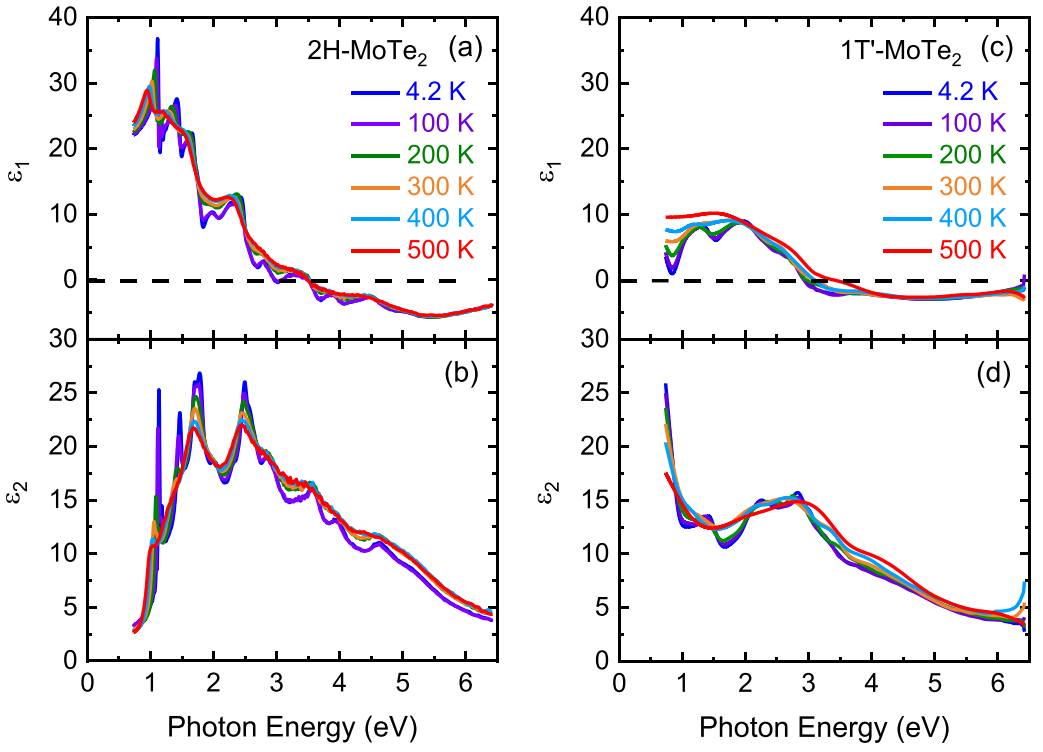

FIG. 2. Temperature-dependent complex dielectric function of (a),(b) 2H- and (c),(d) 1T′-$MoTe_2$.

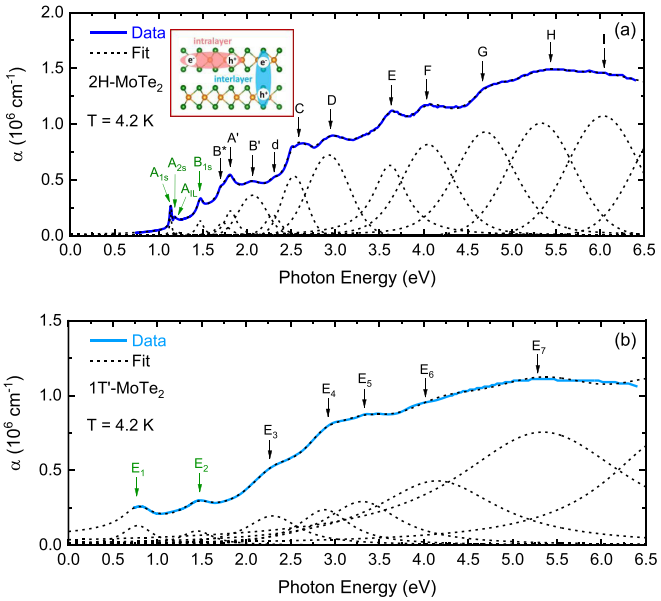

FIG. 3. The optical absorption coefficient spectra of (a) 2H- and (b) 1T′-$MoTe_2$ at 4.2 K with the best fit using the Lorentzian function. The inset of (a) presents the illustration of intralayer and interlayer excitons in 2H-$MoTe_2$.

where r_p and r_s are the amplitude of the reflection coefficient for the p wave and s wave, respectively. The complex dielectric function can be determined from fitting the raw ellipsometric data by building a three medium optical model consisting of single crystal/surface roughness/air ambient. In this study, we take the effects of surface roughness into account through Bruggeman's effective medium approximation [54]. Supplemental Material Figs. 3(a)–3(d) [50] depict the measured Ψ and Δ spectra of 2H- and 1T′-$MoTe_2$ single crystals using variable incident angles θ_i of 55°, 60°, 65°, 70°, and 75°. The experimental data (empty circles) and the fitted model (black dashed lines) agree reasonably well. The surface-roughness values of 2H- and 1T′-$MoTe_2$ are estimated to be 0.78 and 0.87 nm, respectively. Figures 1(b) and 1(c) illustrate the real and imaginary parts of the complex dielectric function at room temperature and at the azimuthal orientation Φ_i of 0°, 45°, and 90°. These spectra are almost identical, indicating that the optical properties of 2H- and 1T′-$MoTe_2$ are isotropic. To perform temperature-dependent spectroscopic ellipsometry measurements between 4.2 and 500 K, we mount 2H- and 1T′-$MoTe_2$ single crystals inside a Janis ST-400 ultrahigh-vacuum, continuous-flow-helium cryostat. All temperature-dependent spectra are measured at $\theta_i = 70°$ and at a base pressure of 10^{-8} torr.

B. Theoretical model

To obtain the complex dielectric function of 2H- and 1T′-$MoTe_2$, we calculate the electronic structure by using the QUANTUM ESPRESSO package [55]. To describe the spin-orbit interaction, we employ the fully relativistic pseudopotentials for Mo and Te atoms from the Optimized Norm-Conserving Vanderbilt Pseudopotential library [56]. A cutoff energy of 60 Ry (816.34 eV) is employed for the plane-wave convergence. The $\boldsymbol{k}$ -point grids are $30 \times 30 \times 4$ and $32 \times 16 \times 4$ in the non-self-consistent calculations for 2H- and 1T′-$MoTe_2$, respectively. All atomic positions and lattice constants are optimized through van der Waals (vdW) correction by using the nonlocal vdW-DF2 functionals [57] for which we select the convergent energy and force thresholds of 0.00001 Ry and 0.0001 Ry/au, respectively.

The real and imaginary parts of complex dielectric functions (ε_1 and ε_2, respectively) as a function of photon energy up to 7 eV are calculated using the YAMBO code [58] and the independent particle approximation (IPA). To obtain the complex dielectric function of the excitonic states, we use YAMBO [59] to solve the Bethe-Salpeter equation (BSE) only for the lower photon-energy region: 0.8–1.6 eV for 2H-$MoTe_2$ and 0.7–2.2 eV for 1T′-$MoTe_2$. In the BSE calculation, we adopt four valence bands and eight (ten) conduction bands near the Fermi energy, with the energy range from −1 (−0.3) to 3 (2.5) eV, as shown in Fig. 10, for 2H-$MoTe_2$ (1T′-$MoTe_2$). These energy ranges are sufficient to enable discussion of the exciton effect in the experimental data presented in Fig. 6(a). In all calculations, the energy band gap of 2H-$MoTe_2$ is corrected on the basis of the experimental data by shifting the energy of the conduction band by 0.433 eV. The optical absorption coefficient $\alpha(\omega)$ is given by ε_1 and ε_2 as follows [60]:

$$\alpha(\omega) = \frac{\sqrt{2}\omega}{c}\left[\sqrt{\varepsilon_1^2(\omega) + \varepsilon_2^2(\omega)} - \varepsilon_1(\omega)\right]^{1/2}, \qquad (2)$$

where c is the speed of light in vacuum and ω is the angular frequency of light.

III. RESULTS AND DISCUSSION

Figure 2 displays the temperature-dependent real (ε_1) and imaginary (ε_2) parts of the complex dielectric function of 2H- and 1T′-$MoTe_2$ through ellipsometric analysis. At room temperature, the ε_1 spectra of 2H- and 1T′-$MoTe_2$ comprise positive values up to approximately 3.0 eV and negative values between 3.0 and 6.0 eV. The optical transitions are identified in the spectra according to resonance and antiresonance features that appeared at the same energy in ε_1 and ε_2, respectively. The ε_2 spectra of 2H- and 1T′-$MoTe_2$ contain several sharp peaks in the range from near-infrared to visible frequency. These absorption peaks are blueshifted with a decrease in temperature.

Figure 3 presents the optical absorption coefficient spectra of 2H- and 1T′-$MoTe_2$ at 4.2 K. We fit the optical absorption peaks and a background using the Lorentzian function. The peak energy of optical absorptions and the corresponding assignments are summarized in Table I. The observed high optical absorption coefficient in the order of 10^6 cm^{-1} is desirable for efficient optical absorbers, such as photodetectors and photocatalysts. For 2H-$MoTe_2$, the literatures [1,42–44] indicate that A_{1s} and B_{1s} can be assigned to intralayer excitonic transitions at the K point, A' and B' are associated with the intralayer excitonic transitions at the Γ point, and C and D are connected to parallel bands near the H point of the Brillouin zone. Notably, within A_{1s} and B_{1s} excitons, we can assign two weak absorption peaks to A_{2s} and A_{IL} at 1.181 ± 0.001 and 1.21 ± 0.01 eV, respectively. The A_{2s} exciton corresponds to the first excited state transition, whereas the A_{IL} exciton

TABLE I. The peak energy of optical absorptions in 2H- and 1T′-$MoTe_2$ at 4.2 K with their corresponding assignments.

$MoTe_2$	Peak energy		Assignment
	Transition	Position (eV)	
2H	A_{1s}	1.136 ± 0.002	$K \to K$
	A_{2s}	1.181 ± 0.001	$K \to K$
	A_{IL}	1.21 ± 0.01	$K \to K$
	B_{1s}	1.469 ± 0.006	$K \to K$
	$B*$	1.701 ± 0.001	$H \to H$
	A'	1.798 ± 0.002	$\Gamma \to \Gamma$
	B'	2.06 ± 0.03	$\Gamma \to \Gamma$
	d	2.295 ± 0.006	$\Gamma \to \Gamma$
	C	2.54 ± 0.04	$H \to H$
	D	2.94 ± 0.01	$H \to H$
	E	3.63 ± 0.01	$M \to M$
	F	4.03 ± 0.01	$M \to M$
	G	4.70 ± 0.07	$K \to K$
	H	5.32 ± 0.01	$K \to K$
	I	6.04 ± 0.02	$K \to K$
1T′	E_1	0.78 ± 0.01	$\Gamma \to \Gamma$
	E_2	1.45 ± 0.01	$Z \to Z$
	E_3	2.30 ± 0.01	$Y \to Y$
	E_4	2.88 ± 0.01	$R \to R$
	E_5	3.30 ± 0.04	$T \to T$
	E_6	4.14 ± 0.08	$U \to U$
	E_7	5.33 ± 0.10	$S \to S$

corresponds to the interlayer excitonic transition. The A_{2s} and A_{IL} peak energies are consistent with those observed in micromagneto reflectance measurements [61]. Furthermore, d is associated with the optical transition caused by the d- and p-orbital mixing induced by increased covalency [46]. E and F excitons are formed in a higher energy range, which contributes to single-particle excitation, the joint density of states of which has a peak [62]. The G, H, and I absorptions are associated with π-electron excitations [63]. For 1T′-$MoTe_2$, E_1 and E_2 are associated with interband transitions at the Γ and Z points [64].

The temperature-dependent optical absorption coefficient spectra of 2H- and 1T′-$MoTe_2$ are presented in Fig. 4. The intensity of optical absorption decreases with increasing temperature for both samples. The positions of the absorption peaks in the spectra of 2H- and 1T′-$MoTe_2$ are redshifted with an increase in temperature. Figure 5 illustrates the energy gap of 2H- and 1T′-$MoTe_2$, respectively, as a function of temperature. The contributions of both direct and indirect band-gap transitions to the optical absorption coefficients can be described by the following expression [65]:

$$\alpha(E) = \frac{A}{E}(E - E_{g,dir})^{0.5} + \frac{B}{E}(E - E_{g,ind} \mp E_{ph})^2, \quad (3)$$

where A and B are constants; $E_{g,\,dir}$ and $E_{g,\,ind}$ represent the direct and indirect band gaps, respectively; and E_{ph} is the phonon energy. The function $\alpha(E)$ enables us to extract the direct and indirect band-gap energies by plotting $(\alpha E)^2$ and $(\alpha E)^{1/2}$ against the photon energy. The temperature-dependent direct band-gap energy of 2H-$MoTe_2$ is presented in Supplemental Material Fig. 4 [50]. At room temperature, the direct band gap at the K point is approximately 1.01 eV, which agrees well with the 1.02–1.10 eV reported in previous experimental studies [26,66,67]. At room temperature, the indirect band-gap energy of 2H-$MoTe_2$ is 0.89 ± 0.01 eV, close to that reported from previous experimental studies [26,36,68,69]. The analysis of the band-gap energy of 1T′-$MoTe_2$ indicates semimetal behavior at all temperatures. In the band structure calculations, the indirect band gap of 2H-$MoTe_2$ is found to occur at Γ-K points of the first Brillouin zone [70], whereas 1T′-$MoTe_2$ exhibits semimetal behavior along the Γ-Y line in the first Brillouin zone [71]. The indirect band gap of 2H-$MoTe_2$ is 0.76 ± 0.01 eV at 500 K and 1.06 ± 0.01 eV at 4.2 K. The temperature-dependent analysis of the indirect band gap in 2H-$MoTe_2$ is plotted in Fig. 5(c). The observed blueshift of the band-gap energy of 2H-$MoTe_2$ with decreasing temperature can be explained using the Bose-Einstein model as follows [72]:

$$E_g(T) = E_g(0) - \frac{2a_B}{\exp\left(\frac{\Theta_B}{T}\right) - 1}, \quad (4)$$

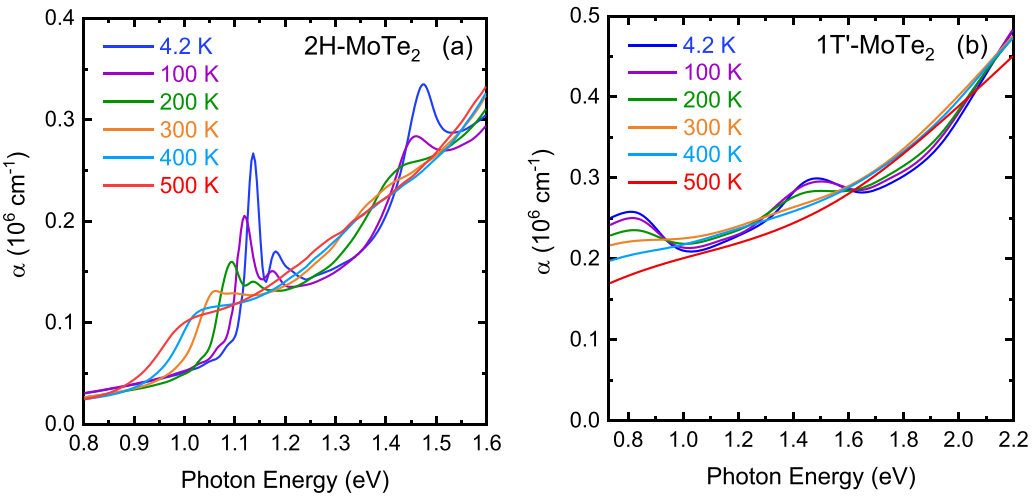

FIG. 4. Temperature-dependent optical absorption coefficient spectra of (a) 2H- and (b) 1T′-$MoTe_2$ at the lower photon-energy range.

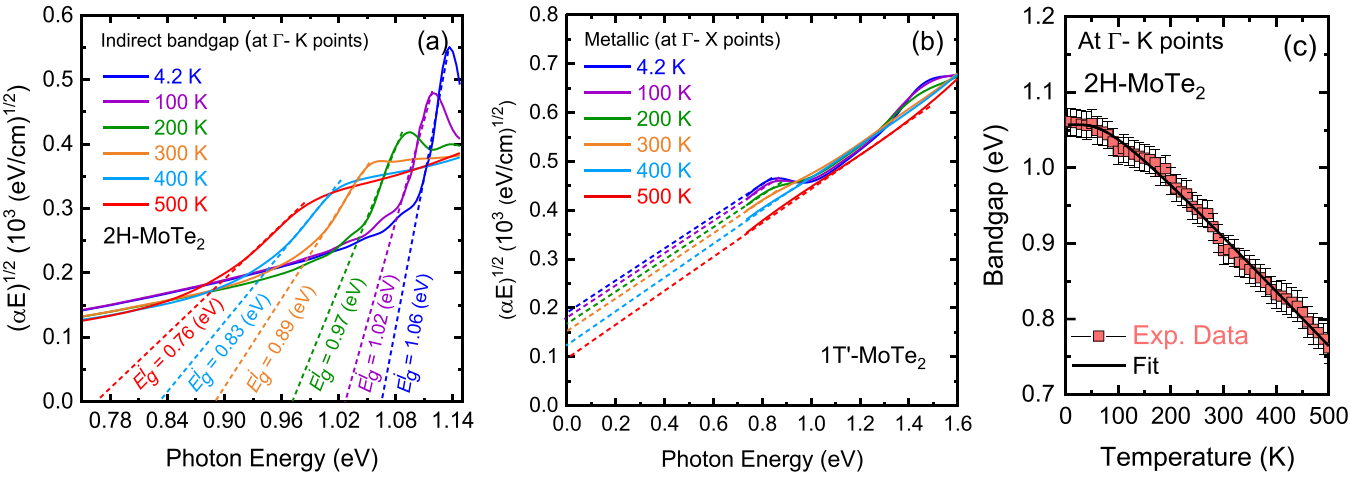

FIG. 5. The extraction of the band gap of (a) 2H- and (b) 1T′-$MoTe_2$ as a function of temperature. (c) Temperature-dependent indirect band gap of 2H-$MoTe_2$. The thin solid line describes the fitting result using the Bose-Einstein model [Eq. (4)].

where $E_g(0)$ is the extrapolated value of the band gap at 0 K, a_B is the strength of the electron-phonon interactions, and Θ_B is the average temperature of phonons. The fitted analyses of $E_g(0)$, a_B, and Θ_B are 1.057 ± 0.002 eV, 82 ± 8 meV, and 222 ± 19 K, respectively. These values are in reasonable agreement with those for other semiconducting TMD materials, such as 2H-MoS_2, 2H-$MoSe_2$, 2H-WS_2, and 2H-WSe_2 single crystals [48]. The comparison of the Bose-Einstein parameters with those of other TMD materials is presented in Supplemental Material Table I [50]. The strength of the electron-phonon interaction discovered herein for 2H-$MoTe_2$ is higher than that in a previous report [48], which may be due to different sample preparation procedures.

The optical absorption coefficient spectra of 2H- and 1T′-$MoTe_2$ at 4.2 K for the lower photon-energy range are displayed in Fig. 6. Other optical absorption coefficient spectra of 2H- and 1T′-$MoTe_2$, obtained at temperatures of 100 to 500 K, are presented in Supplemental Material Figs. 5 and 6 [50]. Four peaks in the spectrum of 2H-$MoTe_2$ are related to the intralayer A_{1s}, A_{2s}, and B_{1s} excitons and the interlayer A_{IL} exciton [Fig. 6(a)]. For 2H-$MoTe_2$, the peak energy of the A_{IL} exciton is higher than that of the A_{2s} exciton, which is the opposite of that found for bulk 2H-MoS_2 [73]. This may be due to 2H-MoS_2 having a larger interlayer exciton binding energy than 2H-$MoTe_2$ [74]. By contrast, we observe two peaks in the spectrum of 1T′-$MoTe_2$, which can be assigned to interband transitions between d orbitals of Mo atoms near the Fermi levels [75] [Fig. 6(b)]. The high density of states is caused by the band crossing near the Γ-Y symmetry for typical Weyl semimetals [75]. We further analyze the valence-band SOC energy of 2H-$MoTe_2$ at the K point. This energy can be determined by considering the energetic separation between the A_{1s} and B_{1s} excitons. Supplemental Material Table II presents SOC energies of 2H-$MoTe_2$, which are comparable to those of other bulk and monolayer TMD materials [50] (see also Refs. [1,76–83] therein). The energy difference between

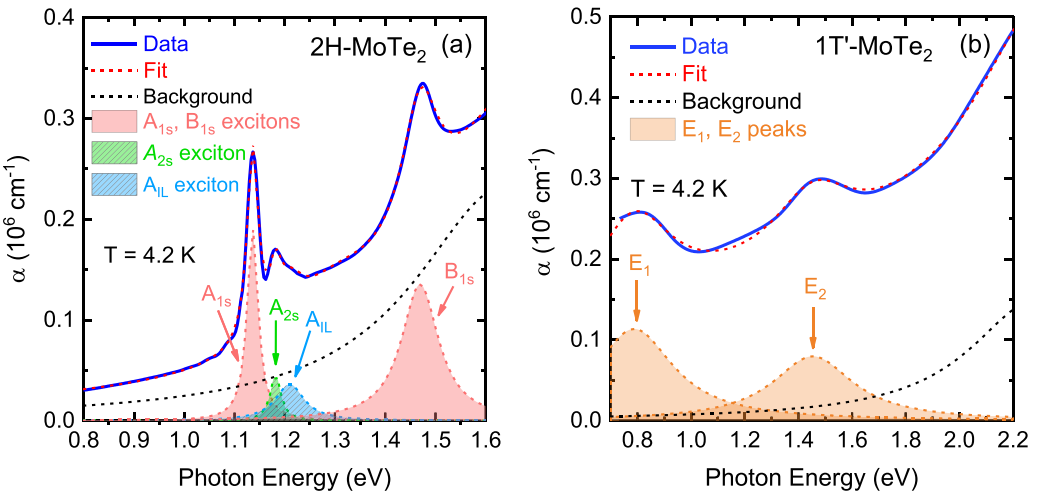

FIG. 6. The optical absorption coefficient spectra of (a) 2H- and (b) 1T′-$MoTe_2$ at 4.2 K for the lower photon-energy range. The dashed lines are the fitting results using the Lorentzian model.

TABLE II. Fitting parameters of the peak energy of the optical transitions in 2H- and 1T′-$MoTe_2$ using the average Bose-Einstein statistical factor [Eq. (5)].

$MoTe_2$	Transition	a (eV)	b (meV)	Θ (K)
2H	A_{1s}	1.212 ± 0.005	75.660 ± 0.005	138.09 ± 12.36
	A_{2s}	1.219 ± 0.002	37.410 ± 0.003	198.27 ± 12.35
	A_{IL}	1.28 ± 0.01	14.92 ± 0.01	185.79 ± 12.95
	B_{1s}	1.489 ± 0.001	20.090 ± 0.001	115.36 ± 6.34
1T′	E_1	0.803 ± 0.003	18.270 ± 0.004	255.43 ± 49.86
	E_2	1.460 ± 0.002	10.410 ± 0.003	164.13 ± 41.66

the A_{1s} and A_{2s} excitons in 2H-$MoTe_2$ is approximately 50 meV, whereas that between the A_{1s} and A_{IL} excitons is approximately 70 meV. These values are larger than those mentioned in a previous experimental report [63].

Figures 7 and 8 compare the temperature-dependent peak position and linewidth of the A_{1s}, A_{2s}, A_{IL}, and B_{1s} excitons in 2H-$MoTe_2$ and the E_1 and E_2 interband transitions in 1T′-$MoTe_2$, respectively. For the excitonic transitions in 2H-$MoTe_2$, the peak energy is redshifted and the linewidth broadens with an increase in temperature. Furthermore, the E_1 and E_2 interband transitions in 1T′-$MoTe_2$ are redshifted and the linewidth broadens with an increase in temperature due to the increased electron-phonon interaction [84]. Since we cannot evaluate the electron-phonon interaction theoretically, we adopt a phenomenological expression of the peak shift and linewidth as a function of temperature as shown below. Notably, the structural phase transition from 2H to 1T′ occurs above 600° C [85,86]. The structural phase transition from 1T′ to $1T_d$ occurs below 250 K [49,87]. We detect no optical signatures of a structural phase transition in 1T′-$MoTe_2$ at low temperatures because the electronic excitations change only a small amount in response to a change in temperature [47]. Thus, we expect that the temperature-dependent behavior reflects an interaction between electrons and phonons. Furthermore, under increasing temperature, the nonlinearity of the peak position and linewidth for the two $MoTe_2$ samples

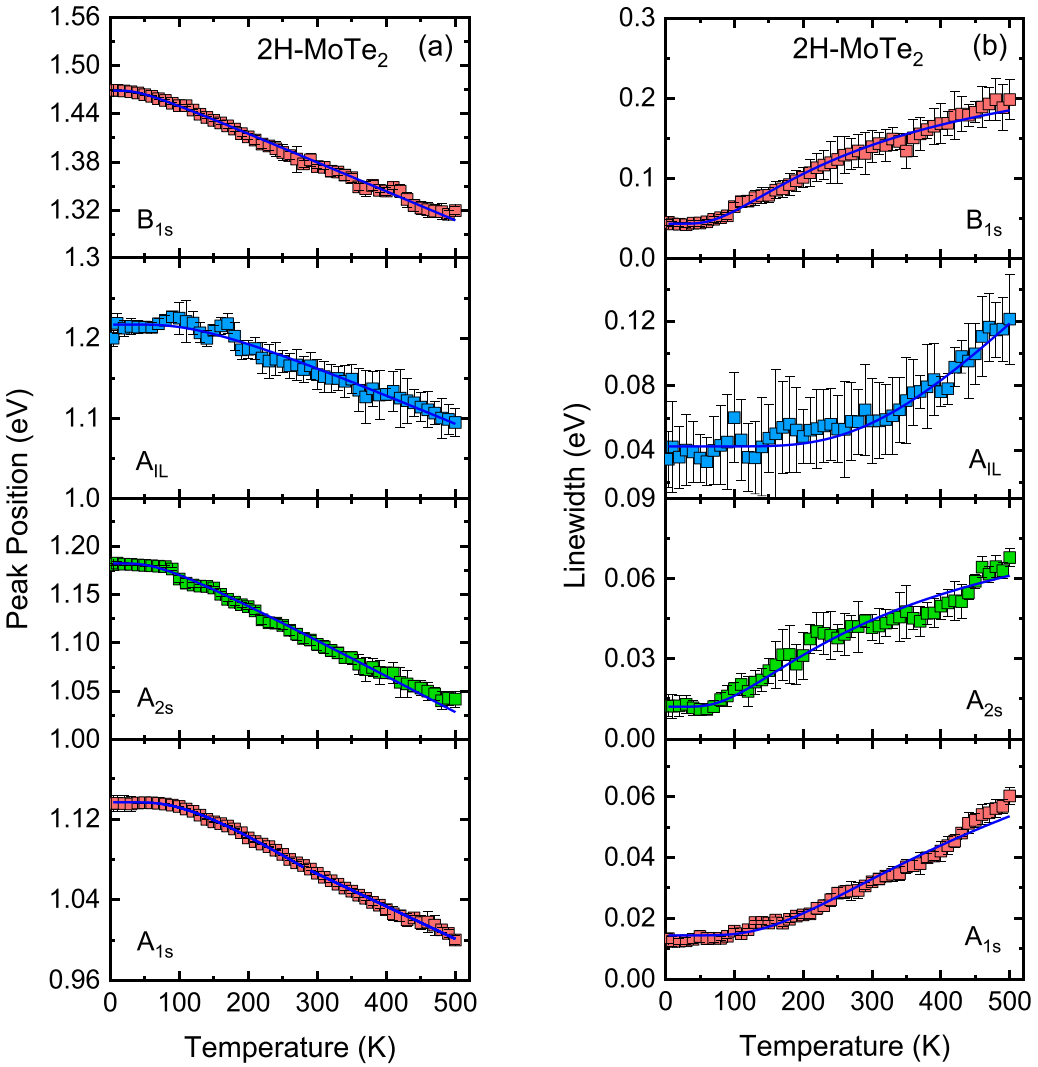

FIG. 7. Temperature-dependent (a) peak position and (b) linewidth of the excitonic transitions in 2H-$MoTe_2$. The thin solid lines denote the fitting results using the Bose-Einstein statistical factor [Eqs. (5) and (6)].

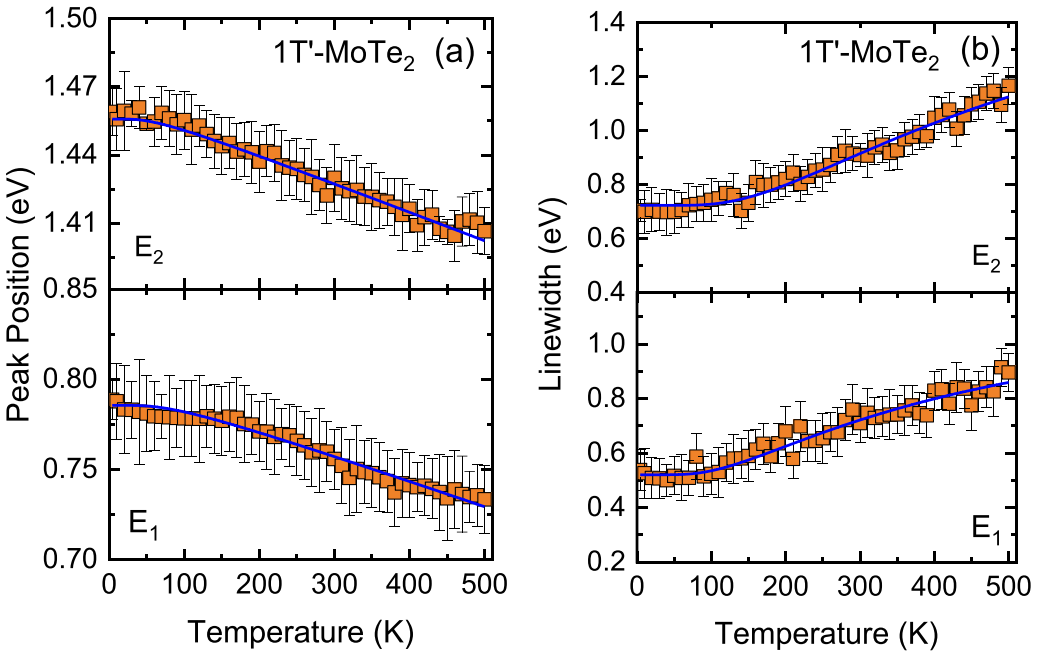

FIG. 8. Temperature-dependent (a) peak position and (b) linewidth of interband transitions in 1T′-$MoTe_2$. The thin solid lines denote the fitting results using the Bose-Einstein statistical factor [Eqs. (5) and (6)].

can be analyzed using the average Bose-Einstein statistical factor [84]:

$$\omega(T) = a - b\left[1 + \frac{2}{e^{(\Theta/T)} - 1}\right] \tag{5}$$

and

$$\Gamma(T) = \Gamma_o\left[1 + \frac{2}{e^{(\Theta/T)} - 1}\right] + \Gamma_1, \tag{6}$$

where a and Γ_1 are the peak energy and linewidth of optical transitions at 0 K, respectively; b and Γ_o represent the strength of the electron-phonon interaction; and Θ is the mean phonon temperature. The thin solid lines in Figs. 7(a), 7(b), 8(a), and 8(b) represent the fitting obtained using Eqs. (5) and (6). The results of the fitting analyses using the average Bose-Einstein statistical factor are summarized in Tables II and III. The values of b and Γ_o describe the energy peak's shift and broadening in the optical absorption spectra with increasing temperature. The energy shift may correspond to a change in the electronic band structure due to the thermal properties of the lattice [85]. The result of a broadening linewidth implies that lifetime of the electronic state decreases with increasing temperature [84]. Moreover, the Γ_o value of 1T′-$MoTe_2$ is larger than that of 2H-$MoTe_2$, which is due to strong free-carrier scattering near the Fermi level [47].

TABLE III. Fitting parameters of the linewidth of the optical transitions in 2H- and 1T′-$MoTe_2$ using the average Bose-Einstein statistical factor [Eq. (6)].

$MoTe_2$	Transition	Γ_1 (eV)	Γ_o (meV)	Θ (K)
2H	A_{1s}	0.105 ± 0.009	60.021 ± 0.004	261.64 ± 20.33
	A_{2s}	0.079 ± 0.004	50.565 ± 0.002	310.26 ± 22.39
	A_{IL}	0.086 ± 0.002	45.521 ± 0.002	239.88 ± 18.29
	B_{1s}	0.201 ± 0.006	122.320 ± 0.003	273.85 ± 17.53
1T′	E_1	0.22 ± 0.05	222.33 ± 0.05	392.52 ± 34.74
	E_2	0.062 ± 0.001	311.32 ± 0.05	355.41 ± 39.31

The calculated electronic band structure of 2H- and 1T′-$MoTe_2$ is displayed in Figs. 9(a) and 9(b), respectively. The calculated valence bands are in agreement with the results of angle-resolved photoemission spectroscopic measurements for 2H- and 1T′-$MoTe_2$ [88,89]. For 2H-$MoTe_2$, $\Delta E_{SO} = 285$ meV is found at the K point; this value is close to the experimental value of $\Delta E_{SO} = 333$ meV. By contrast, $\Delta E_{SO} = 65$ meV is found near the Γ point for 1T′-$MoTe_2$. In addition, the electronic band structures show that 2H-$MoTe_2$ is a semiconductor with an indirect band gap of 0.627 eV, whereas 1T′-$MoTe_2$ is a semimetal. Notably, 1T′-$MoTe_2$ has a small gap of approximately 40 meV near the Γ point. For 2H-$MoTe_2$, the theoretical value of the indirect band gap of 0.627 eV is smaller than the experimental value of 1.06 eV [Fig. 5(c)] because the BSE functional often underestimates band-gap values. Therefore, we employ a band-gap correction of approximately 0.433 eV for calculating the optical properties of 2H-$MoTe_2$.

To confirm the accuracy of the complex dielectric function (ε_1 and ε_2) and optical absorption coefficient spectra $\alpha(\omega)$ in Figs. 2 and 3, respectively, we first calculate ε_1, ε_2, and $\alpha(\omega)$ for 2H- and 1T′-$MoTe_2$ by using IPA, as shown in Figs. 9(c) and 9(d). Within the IPA method, we calculate the optical properties for photon energy up to 6.5 eV. For photon energy larger than 2 eV, the exciton effect is discovered to be absent in the observed optical absorption spectra.

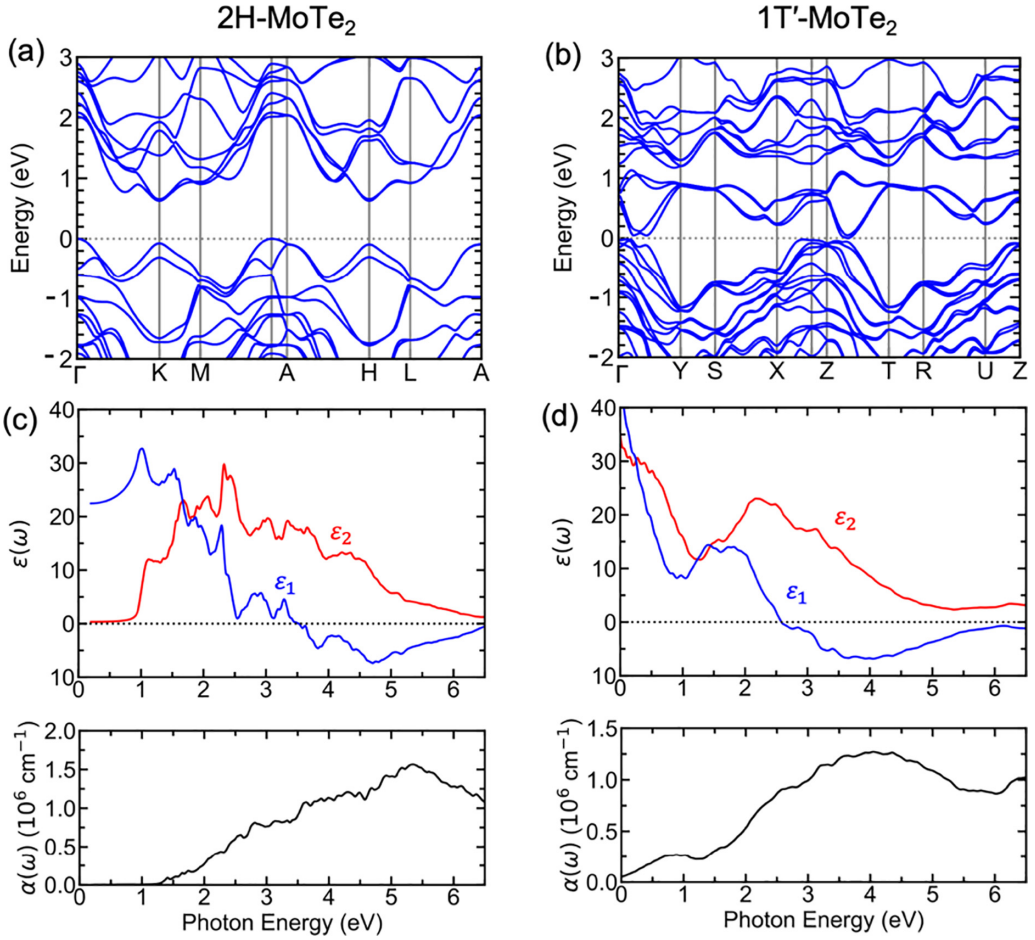

FIG. 9. The calculated electronic band structures of (a) 2H- and (b) 1T′-$MoTe_2$ (b), respectively. The complex dielectric function (ε_1 and ε_2) and the optical absorption coefficient spectra $\alpha(\omega)$ of (c) 2H- and (d) 1T′-$MoTe_2$ with the independent particle approximation.

Therefore, the IPA is suitable for reproducing the experiment involving high photon energy. For 2H-$MoTe_2$, the theoretical values [$\varepsilon_1 = 0$, $\varepsilon_2 = 18$, and $\alpha(\omega) = 0.85 \times 10^6\,\mathrm{cm}^{-1}$ at 3.5 eV] agree well with the experimental values [$\varepsilon_1 = 0$, $\varepsilon_2 = 17$, and $\alpha(\omega) = 0.9 \times 10^6\,\mathrm{cm}^{-1}$ at 3.5 eV]. This is also the case for the theoretical values [$\varepsilon_1 = 0$, $\varepsilon_2 = 20$, and $\alpha(\omega) = 0.80 \times 10^6\,\mathrm{cm}^{-1}$ at 2.6 eV] and experimental values [$\varepsilon_1 = 0$, $\varepsilon_2 = 15$, and $\alpha(\omega) = 0.80 \times 10^6\,\mathrm{cm}^{-1}$ at 2.9 eV] for 1T′-$MoTe_2$.

To reproduce the exciton peaks at low photon energy shown in Figs. 6(a) and 6(b), we calculate $\alpha(\omega)$ using the BSE, as depicted in Figs. 10(a) and 10(b). The BSE method is an expensive calculation compared with the IPA method. Therefore, the BSE method is suitable only for low photon energy, in which case only a few low-energy bands need to be considered. For 2H-$MoTe_2$, the BSE method reveals two exciton peaks (A_{1s}: 0.24×10^6 and B_{1s}: $0.37 \times 10^6\,\mathrm{cm}^{-1}$) at 1.15 and 1.4 eV, which are comparable with the experimental peaks (A_{1s}: 0.27×10^6 and B_{1s}: $0.37 \times 10^6\,\mathrm{cm}^{-1}$) at 1.14 and 1.47 eV. We note that the A_{2s} and A_{IL} excitons are not reproduced in our calculations because the energy splitting between these peaks is small at approximately 50 meV and a large number of $\boldsymbol{k}$ points would thus be required. For 1T′-$MoTe_2$, the difference between the BSE and IPA findings is slight. Therefore, the exciton effect in 1T′-$MoTe_2$ is weaker than that in 2H-$MoTe_2$.

IV. SUMMARY

The temperature-dependent complex dielectric function and optical absorption coefficient spectra of 2H- and 1T′-$MoTe_2$ single crystals are investigated herein using spectroscopic ellipsometry and first-principles calculations. The optical absorption spectra obtained at 4.2 K confirm that 2H-$MoTe_2$ has an indirect band gap of 1.06 ± 0.01 eV, whereas 1T′-$MoTe_2$ exhibits semimetal behavior. Furthermore, we find three distinct intralayer A_{1s}, A_{2s}, and B_{1s} excitons and one interlayer A_{IL} exciton at 1.136 ± 0.002, 1.181 ± 0.001, 1.469 ± 0.006, and 1.21 ± 0.01 eV in 2H-$MoTe_2$. The SOC energy of 2H-$MoTe_2$ is 333 meV. By contrast, we discover two broad interband transitions at 0.78 ± 0.01 and 1.45 ± 0.01 eV in 1T′-$MoTe_2$. These two optical absorptions shift to lower energy with an increase in temperature, indicating the increased electron-phonon interaction. These results provide insight into the complex nature of optical transitions in 2H- and 1T′-$MoTe_2$ and can be utilized in technological applications for $MoTe_2$-based optoelectronic and photonic devices.

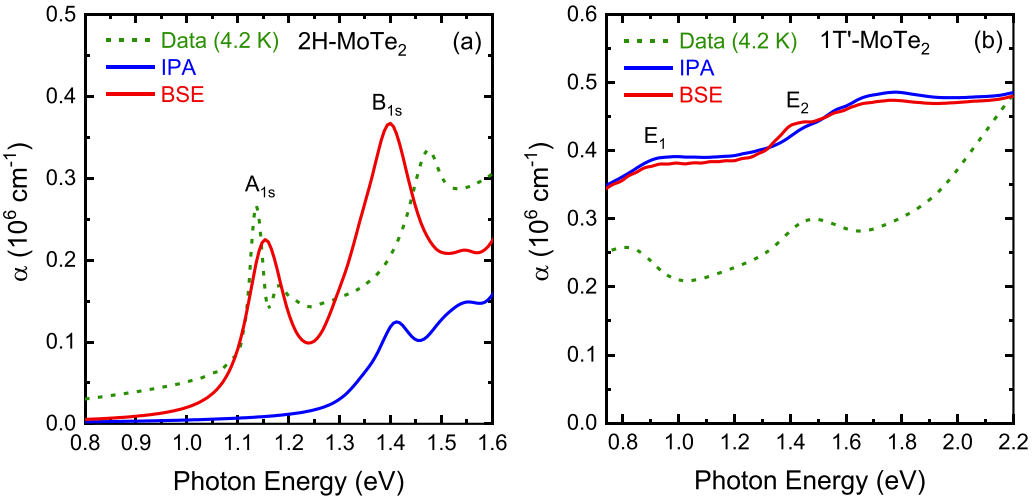

FIG. 10. The calculated optical absorption coefficient $\alpha(\omega)$ of (a) 2H- and (b) 1T′-$MoTe_2$ with the Bethe-Salpeter equation (BSE, red solid line) and independent particle approximation (IPA, blue solid line). The experiment data at 4.2 K is also shown as a green dashed line for comparison.

The data that support the findings of this study are available from the corresponding author upon reasonable request.

ACKNOWLEDGMENTS

H.-L.L. thanks the Ministry of Science and Technology of the Republic of China for its financial support under Grant No. MOST 111-2112-M-003-016. R. Sankar acknowledges Academia Sinica for support under Grant No. AS-iMATE-111-12 and the Ministry of Science and Technology of the Republic of China for support under Grants No. MOST 110-2124-M-001-009-MY3 and No. MOST 110-2112-M-001-065-MY3 of Taiwan. R. Saito acknowledges JSPS KAKENHI for support under Grants No. JP18H01810 and No. JP22H00283. N.T.H. acknowledges JSPS KAKENHI for support under Grant No. JP20K15178.

H.-L.L. conceived the research and was responsible for the experimental design. D.P.G. conducted the experiments. R. Sankar was responsible for the sample preparation. N.T.H. and R. Saito performed the first-principles calculations and theoretical analyses. D.P.G., H.-L.L., N.T.H., and R. Saito drafted the paper. All contributing authors have discussed the results and provided their comments regarding the manuscript.

The authors declare no competing interests.

[1] C. Ruppert, O. B. Aslan, and T. F. Heinz, Optical properties and band gap of single- and few-layer $MoTe_2$ crystals, Nano Lett. **14**, 6231 (2014).

[2] D. E. Aspnes, Spectroscopic ellipsometry—Past, present, and future, Thin Solid Films **571**, 334 (2014).

[3] H. Fujiwara, *Spectroscopy Ellipsometry: Principles and Applications* (Wiley, New York, 2007).

[4] J. N. Hilfiker, N. Hong, and S. Schoeche, Mueller matrix spectroscopic ellipsometry, Adv. Opt. Technol. **11**, 59 (2022).

[5] R. Wang, Y. Yu, S. Zhou, H. Li, H. Wong, Z. Luo, L. Gan, and T. Zhai, Strategies on phase control in transition metal dichalcogenides, Adv. Funct. Mater. **28**, 1802473 (2018).

[6] H. H. Huang, X. Fan, D. J. Singh, and W. T. Zheng, Recent progress of TMD nanomaterials: Phase transitions and applications, Nanoscale **12**, 1247 (2020).

[7] H. Yang, S. W. Kim, M. Chhowalla, and Y. H. Lee, Structural and quantum-state phase transition in van der Waals layered materials, Nat. Phys. **13**, 931 (2017).

[8] T. Rao, H. Wang, Y. J. Zeng, Z. Guo, H. Zhang, and W. Liao, Phase transitions and water splitting applications of 2D transition metal dichalcogenides and metal phosphorous trichalcogenides, Adv. Sci. **8**, 20022284 (2021).

[9] S. Manzeli, D. Ovchinnikov, D. Pasquier, O. V. Yazyev, and A. Kis, 2D transition metal dichalcogenides, Nat. Rev. Mater. **2**, 17033 (2017).

[10] J. Kim and Z. Lee, Phase transformation of two-dimensional transition metal dichalcogenides, Appl. Microsc. **48**, 43 (2018).

[11] W. Li, X. Qian, and J. Li, Phase transitions in 2D materials, Nat. Rev. **6**, 829 (2021).

[12] W. Zhao, J. Pan, Y. Fang, X. Che, D. Wang, K. Bu, and F. Huang, Metastable MoS_2: Crystal structure, electronic band structure, synthetic approach and intriguing physical properties, Chem. Eur. J. **24**, 15942 (2018).

[13] Y. Yu, G. H. Nam, Q. He, X. J. Wu, K. Zhang, Z. Yang, J. Chen, Q. Ma, M. Zhao, Z. Liu, F. R. Ran, X. Wang, H. Li, X. Huang, B. Li, Q. Xiong, Q. Zhang, Z. Liu, L. Gu, Y. Du, W. Huang, and H. Zhang, High phase-purity 1T′-MoS_2- and 1T′-$MoSe_2$-layered crystals, Nat. Chem. **10**, 638 (2018).

[14] E. D. Hanson, L. M. Lilley, J. D. Cain, S. Hao, E. Palacios, K. Aydin, C. Wolverton, T. Meade, and V. P. Dravid, Phase engineering and optical properties of 2D $MoSe_2$: Promise and pitfalls, Mater. Chem. Phys. **225**, 219 (2019).

[15] M. S. Sokolikova, Peter C. Sherrell, P. Palczynski, V. L. Bemmer, and C. Mattevi, Direct solution-phase synthesis of 1T'-WSe_2 nanosheets, Nat. Commun. **10**, 712 (2019).

[16] G. J. Orchin, D. De Fazio, A. Di Bernardo, M. Hamer, Yoon D, A. A. Cadore, I. Goykhman, K. Watanabe, T. Taniguchi, J. W. A. Robinson, R. V. Gorbanchev, A. C. Ferrari, and R. H. Hadfield, Niobium diselenide superconducting photodetectors, Appl. Phys. Lett **114**, 251103 (2019).

[17] C. Wang, F. Yang, and Y. Gao, The highly-efficient light-emitting diodes based on transition metal dichalcogenides: From architecture to performance, Nanoscale Adv. **2**, 4323 (2020).

[18] G. H. Lee, T. V. Cuong, D. K. Yeo, H. Cho, B. D. Ryu, E. M. Kim, T. S. Nam, E. K. Suh, T. H. Seo, and C. H. Hong, Hexagonal boron nitride passivation layer for improving the performance and reliability of InGaN/GaN light-emitting diodes, Appl. Sci. **11**, 9321 (2021).

[19] B. Xu, C. Zhi, and P. Shi, Latest advances in MXene biosensors, J. Phys. Mater. **3**, 031001 (2020).

[20] K. Shavanova, Y. Bakakina, I. Burkova, I. Shtepliuk, R. Viter, A. Ubelis, V. Beni, N. Starodub, R. Yakimova, and V. Khranovskyy, Application of 2D non-graphene materials and 2D oxide nanostructures for biosensing technology, Sensors **16**, 223 (2016).

[21] B. Munkhbat, P. Wrobel, T. J. Antosiewicz, and T. O. Shegai, Optical constants of several multilayer transition metal dichalcogenides measured by spectroscopic ellipsometry in the 300–1700 nm range: High index, anisotropy, and hyperbolicity, ACS Photonics **9**, 2398 (2022).

[22] A. Laturia, M. L. V. de Put, and W. G. Vandenberghe, Dielectric properties of hexagonal boron nitride and transition metal dichalcogenides: From monolayer to bulk, npj 2D Mater. Appl. **2**, 6 (2018).

[23] C. Shang, Y. Q. Fang, N. Z. Wang, Y. F. Wang, Z. Liu, B. Lei, F. B. Meng, L. K. Ma, T. Wu, Z. F. Wang, C. G. Zeng, F. Q. Huang, Z. Sun, and X. H. Chen, Superconductivity in the metastable $1T'$ and $1T'''$ phases of MoS_2 crystals, Phys. Rev. B **98**, 184513 (2018).

[24] Q. Ji, C. Li, J. Wang, J. Niu, Y. Gong, Z. Zhang, Q. Fang, Y. Zhang, J. Shi, L. Liao, X. Wu, L. Gu, Z. Liu, and Y. Zhang, Metallic vanadium disulfide nanosheets as a platform material for multifunctional electrode applications, Nano Lett. **17**, 4908 (2017).

[25] W. G. Dawson and D. W. Bullett, Electronic structure and crystallography of $MoTe_2$ and WTe_2, J. Phys. C: Solid State Phys. **20**, 6159 (1987).

[26] I. G. Lezama, A. Ubaldini, M. Longobardi, E. Giannini, C. Renner, A. B. Kuzmenko, and A. F. Morpurgo, Surface transport and band gap structure of exfoliated 2H-$MoTe_2$ crystals, 2D Mater. **1**, 021002 (2014).

[27] J. Gusakova, X. Wang, L. L. Shiau, A. Krivosheeva, V. Shaposhnikov, V. Borisenko, V. Gusakov, and B. K. Tay, Electronic properties of bulk and monolayer TMDs: Theoretical study within DFT framework (GVJ-2e method), Phys. Status Solidi A **214**, 1700218 (2017).

[28] I. G. Lezama, A. Arora, A. Ubaldini, C. Barreteau, E. Giannini, M. Potemski, and A. F. Morpurgo, Indirect-to-direct band gap crossover in few-layer $MoTe_2$, Nano Lett. **15**, 2336 (2015).

[29] J. H. Kim, M. R. Bergren, J. C. Park, S. Adhikari, M. Lorke, T. Frauenheim, D. H. Choe, B. Kim, H. Choi, T. Gregorkiewicz, and Y. H. Lee, Carrier multiplication in van der Waals layered transition metal dichalcogenides, Nat. Commun. **10**, 5488 (2017).

[30] Y. Zhu, Z. Li, L. Zhang, B. Wang, Z. Luo, J. Long, J. Yang, L. Fu, and Y. Lu, High-efficiency monolayer molybdenum ditelluride light-emitting diode and photodetector, ACS Appl. Mater. Interfaces **10**, 43291 (2018).

[31] Y. Li, J. Zhang, D. Huang, H. Sun, F. Fan, J. Feng, Z. Wang, and C. Z. Ning, Room-temperature continuous-wave lasing from monolayer molybdenum ditelluride integrated with a silicon nanobeam cavity, Nat. Nanotechnol. **12**, 987 (2017).

[32] S. Hussain, S. A. Patil, D. Vikraman, N. Mengal, H. Liu, W. Song, K. S. An, S. H. Jeong, H. S. Kim, and J. Jung, Large area growth of $MoTe_2$ films as high performance counter electrodes for dye-sensitized solar cells, Sci. Rep. **8**, 29 (2018).

[33] E. Wu, Y. Xie, B. Yuan, H. Zhang, X. Hu, J. Liu, and D. Zhang, Ultrasensitive and fully reversible NO_2 gas sensing based on p-type $MoTe_2$ under ultraviolet illumination, ACS Sens. **3**, 1719 (2018).

[34] H. P. Hughes and R. H. Friend, Electrical resistivity anomaly in β-$MoTe_2$ (metallic behavior), J. Phys. C: Solid State Phys. **11**, 1978 (1978).

[35] R. Clarke, E. Maeseglia, and H. P. Hughes, A low-temperature structural phase transition in β-$MoTe_2$, Philos. Mag. B **38**, 121 (1978).

[36] D. H. Keum, S. Cho, J. H. Kim, D. H. Choe, H. J. Sung, M. Kan, H. Kang, J. Y. Hwang, S. W. Kim, H. Yang, K. J. Chang, and Y. H. Lee, Bandgap opening in few-layered monoclinic $MoTe_2$, Nat. Phys. **11**, 482 (2015).

[37] P. Song, C. Hsu, M. Zhao, X. Zhao, T. R. Chang, J. Teng, H. Lin, and K. P. Loh, Few-layer $1T'$-$MoTe_2$ as gapless semimetal with thickness dependent carrier transport, 2D Mater. **5**, 031010 (2018).

[38] X. Qian, J. Liu, L. Fu, and J. Li, Quantum spin Hall effect in two-dimensional transition metal dichalcogenides, Science **346**, 1344 (2014).

[39] Z. Wang, B. J. Wieder, J. Li, B. Yan, and B. A. Bernevig, Higher-Order Topology, Monopole Nodal Lines, and the Origin of Large Fermi Arcs in Transition Metal Dichalcogenides XTe_2 (X = Mo, W), Phys. Rev. Lett. **123**, 186401 (2019).

[40] Y. Qi, P. G. Naumov, M. N. Ali, C. R. Rajamathi, W. Schnelle, O. Barkalov, M. Hanfland, S. C. Wu, C. Shekhar, Y. Sun, V. Sub, M. Scmidt, U. Schwarz, E. Pippel, P. Werner, R. Hillebrand, T. Forster, E. Kampert, S. Parkin, R. J. Cava, C. Felser, B. Yan, and S. A. Medvedev, Superconductivity in Weyl semimetal candidate $MoTe_2$, Nat. Commun. **7**, 11038 (2016).

[41] Y. Li, A. Singh, S. Krylyuk, A. Davydov, and R. Jaramillo, Near-infrared photonic phase-change properties of transition metal ditellurides, in *Low-Dimensional Material and Devices*, edited by N. P. Kobayashi, A. A. Talin, A. V. Davydov (SPIE, San Diago, California, 2019).

[42] R. Oliva, T. Wozniak, F. Dybala, J. Kopaczek, P. Scharoch, and R. Kudrawiec, Hidden spin-polarized bands in semiconducting 2H-$MoTe_2$, Mater. Res. Lett. **8**, 75 (2020).

[43] W. Zheng, M. Bonn, and H. I. Wang, Photoconductivity multiplication in semiconducting few-layer $MoTe_2$, Nano Lett. **20**, 5807 (2020).

[44] F. Lahourpour, A. Boochani, S. S. Parhizgar, and S. M. Elahi, Structural, electronic and optical properties of graphene-like

nano-layers MoX_2 (X: S, Se, Te): DFT study, J. Theor. Appl. Phys. **13**, 191 (2019).

[45] B. Davey and B. L. Evans, The optical properties of $MoTe_2$ and WSe_2, Phys. Status Solidi A **13**, 483 (1972).

[46] A. R. Beal, J. C. Knights, and W. Y. Liang, Transmission spectra of some transition metal dichalcogenides: II. Group VIA: Trigonal prismatic coordination, J. Phys. C: Solid State Phys. **5**, 3540 (1972).

[47] S-i. Kimura, Y. Nakajima, Z. Mita, R. Jha, R. Higashinaka, T. D. Matsuda, and Y. Aoki, Optical evidence of the type-II Weyl semimetals $MoTe_2$ and WTe_2, Phys. Rev. B. **99**, 195203 (2019).

[48] J. Kopaczek, S. Zelewski, K. Yumigeta, R. Sailus, S. Tongay, and R. Kudrawiec, Temperature dependence of the indirect gap and the direct optical transitions at the high-symmetry point of the Brillouin zone and band nesting in MoS_2, $MoSe_2$, $MoTe_2$, WS_2, and WSe_2 crystals, J. Phys. Chem. C. **126**, 5665 (2022).

[49] R. Sankar, G. N. Rao, I. P. Muthuselvam, C. Butler, N. Kumar, G. S. Murugan, C. Shekhar, T. R. Chang, C. Y. Wen, C. W. Chen, W. L. Lee, M. T. Lin, H. T. Jeng, C. Felser, and F. C. Chou, Polymorphic layered $MoTe_2$ from semiconductor, topological insulator, to Weyl semimetal, Chem. Mater. **29**, 699 (2017).

[50] See Supplemental Material at http://link.aps.org/supplemental/10.1103/PhysRevMaterials.7.044001 for supporting information of our results, including characterization (XRD and Raman measurements) and optical features of 2H- and 1T′-$MoTe_2$ single crystals.

[51] D. P. Gulo, H. Yeh, W. H. Chang, and H. L. Liu, Temperature-dependent optical and vibrational properties of $PtSe_2$ thin films, Sci. Rep. **10**, 19003 (2020).

[52] S. Paul, S. Karak, A. Mathew, A. Ram, and S. Saha, Electron-phonon and phonon-phonon anharmonic interactions in 2H-MoX_2 (X = S, Te): A comprehensive resonant Raman study, Phys. Rev. B **104**, 075418 (2021).

[53] J. P. Fraser, L. Masaityte, J. Zhang, S. Laing, J. C. M. Lopez, A. F. McKenzie, J. C. McGlynn, V. Panchal, D. Graham, O. Kazakova, T. Pichler, D. A. MacLaren, D. A. J. Moran, and A. Y. Ganin, Selective phase growth and precise-layer control in $MoTe_2$, Commun. Mater. **1**, 48 (2020).

[54] D. Lehmann, F. Seidel, and D. R. T. Zahn, Thin films with high surface roughness: Thickness and dielectric function analysis using spectroscopic ellipsometry, SpringerPlus **3**, 82 (2014).

[55] P. Giannozzi, S. Baroni, N. Bonini, M. Calandra, R. Car, C. Cavazzoni, D. Ceresoli, G. L. Chiarotti, M. Cococcioni, I. Dabo *et al.*, Quantum ESPRESSO: A modular and open-source software project for quantum simulations of materials, J. Phys.: Condens. Matter **21**, 395502 (2009).

[56] D. R. Hamann, Optimized norm-conserving Vanderbilt pseudopotentials, Phys. Rev. B **88**, 085117 (2013).

[57] K. Lee, É. D. Murray, L. Kong, B. I. Lundqvist, and D. C. Langreth, Higher-accuracy van der Waals density functional, Phys. Rev. B **82**, 081101(R) (2010).

[58] A. Marini, C. Hogan, M. Grüning, and D. Varsano, yambo: An *ab initio* tool for excited state calculations, Comput. Phys. Commun. **180**, 1392 (2019).

[59] D. Sangalli, A. Ferretti, H. Miranda, C. Attaccalite, I. Marri, E. Cannuccia, P. Melo, M. Marsili, F. Paleari, A. Marrazzo *et al.*, Many-body perturbation theory calculations using the yambo code, J. Phys.: Condens. Matter. **31**, 325902 (2019).

[60] N. T. Hung, A. R. T. Nugraha, and R. Saito, *Quantum ESPRESSO Course for Solid-State Physics* (Jenny Stanford Publishing, United Square, Singapore, 2022).

[61] A. Arora, M. Druppel, R. Schmidt, T. Deilmann, R. Schneider, M. R. Molas, P. Marauhn, S. M. de Vasconcellos, M. Potemski, M. Rohlfing, and R. Bratschitsch, Interlayer excitons in a bulk van der Waals semiconductor, Nat. Commun. **8**, 639 (2017).

[62] M. Fang, H. Gu, Z. Guo, J. Liu, L. Huang, and S. Liu, Temperature and thickness dependent dielectric functions of $MoTe_2$ thin films investigated by spectroscopic ellipsometry, Appl. Surf. Sci. **605**, 154813 (2022).

[63] V. Grasso, G. Mondio, and G. Saitta, Optical constants of $MoTe_2$ from reflectivity measurements. (Brillouin zone transitions), J. Phys. C: Solid State Phys. **5**, 1101 (1972).

[64] A. Popescu, A. Pertsova, A. V. Balatsky, and L. M. Woods, Optical response of $MoTe_2$ and WTe_2 Weyl semimetals: Distinguishing between bulk and surface contributions, Adv. Theory Simul. **3**, 1900247 (2020).

[65] J. I. Pankove, *Optical Processes in Semiconductors* (Springer, New York, 1971).

[66] S. J. Zelewski and R. Kudrawiec, Photoacoustic and modulated reflectance studies of indirect and direct band gap in van der Waals crystals, Sci. Rep. **7**, 15365 (2017).

[67] E. Jung, J. C. Park, Y. S. Seo, J. H. Kim, J. Hwang, and Y. H. Lee, Unusually large exciton binding energy in multilayered 2H-$MoTe_2$, Sci. Rep. **12**, 4543 (2022).

[68] G. Froehlicher, E. Lorchat, and S. Berciaud, Direct versus indirect band gap emission and exciton-exciton annihilation in atomically thin molybdenum ditelluride ($MoTe_2$), Phys. Rev. B **94**, 085429 (2016).

[69] C. Cong, Y. Zhang, W. Chen, J. Chu, T. Lei, J. Pu, L. Dai, C. Wu, Y. Cheng, T. Zhai *et al.*, Electronic and optoelectronic applications based on 2D novel anisotropic transition metal dichalcogenides, Adv. Sci. **4**, 1700231 (2017).

[70] J. Wu, L. Meng, J. Yu, and Y. Li, A first-principles study of electronic properties of twisted $MoTe_2$, Phys. Status Solidi B **257**, 1900412 (2020).

[71] H. J. Kim, S. H. Kang, I. Hamada, and Y. W. Son, Origins of the structural phase transitions in $MoTe_2$ and WTe_2, Phys. Rev. B **95**, 180101(R) (2017).

[72] K. P. O'Donnell and X. Chen, Temperature dependence of semiconductor band gaps, Appl. Phys. Lett. **58**, 2924 (1991).

[73] A. Arora, T. Deilmann, P. Marauhn, M. Druppel, R. Schneider, M. R. Molas, D. Vaclavkova, S. M. de Vasconcellos, M. Rohlfing, M. Potemski, and R. Bratschitsch, Valley-contrasting optics of interlayer excitons in Mo- and W-based bulk transition metal dichalcogenides, Nanoscale **10**, 15571 (2018).

[74] I. C. Gerber, E. Courtade, S. Shree, C. Robert, T. Taniguchi, K. Watanabe, A. Balocchi, P. Renucci, D. Lagarde, X. Marie, and B. Urbaszek, Interlayer excitons in bilayer MoS_2 with strong oscillator strength up to room temperature, Phys. Rev. B. **99**, 035443 (2019).

[75] M. Dadsetani and A. Ebrahimian, Optical distinctions between Weyl semimetal TaAs and Dirac semimetal Na_3Bi: An *ab initio* investigation, J. Electron. Mater. **45**, 5867 (2016).

[76] W. Li, A. G. Birdwell, M. Amani, R. A. Burke, X. Ling, Y. H. Lee, X. Liang, L. Peng, C. A. Richter, J. Kong *et al.*, Broadband optical properties of large-area monolayer CVD molybdenum disulfide, Phys. Rev. B **90**, 195434 (2014).

[77] N. Saigal and S. Ghosh, H-point exciton transitions in bulk MoS_2, Appl. Phys. Lett. **106**, 182103 (2015).

[78] H. L. Liu, C. C. Shen, S. H. Su, C. L. Hsu, M. Y. Li, and L. J. Li, Optical properties of monolayer transition metal dichalcogenides probed by spectroscopic ellipsometry, Appl. Phys. Lett. **105**, 201905 (2014).

[79] J. Kopaczek, M. P. Polak, P. Scharoch, K. Wu, B. Chen, S. Tongay, and R. Kudrawiec, Direct optical transitions at K- and H-point of Brillouin zone in bulk MoS_2, $MoSe_2$, WS_2, and WSe_2, J. Appl. Phys. **119**, 235705 (2016).

[80] M. Dendzik, M. Michiardi, C. Sanders, M. Bianchi, J. A. Miwa, S. S. Gronborg, J. V. Lauritsen, A. Bruix, B. Hammer, and P. Hofmann, Growth and electronic of epitaxial single-layer WS_2 on Au (111), Phys. Rev. B **92**, 245442 (2015).

[81] R. Huisman, R. de Jonge, and C. H. F. Jellinek, Trigonal-prismatic coordination in solid compounds of transition metals, J. Solid State Chem. **3**, 56 (1971).

[82] Y. Zhang, M. M. Ugeda, C. Jin, S. F. Shi, A. J. Bradley, A. M. Recio, H. Ryu, J. Kim, S. Tang, Y. Kim *et al.*, Electronic structure, surface doping, and optical response in epitaxial WSe_2 thin films, Nano Lett. **16**, 2485 (2016).

[83] R. F. Frindt, The optical properties of single crystals of WSe_2 and $MoTe_2$, J. Phys. Chem. Solids **24**, 1107 (1963).

[84] P. Lautenschlager, M. Garriga, L. Vina, and M. Cardona, Temperature dependence of the dielectric function and interband critical points in silicon, Phys. Rev. B **36**, 4821 (1987).

[85] D. Rhodes, D. A. Chenet, B. E. Janicek, C. Nyby, Y. Lin, W. Jin, D. Edelberg, E. Mannebach, N. Finney, A. Antony *et al.*, Engineering the structural and electronic phases of $MoTe_2$ through W substitution, Nano Lett. **17**, 1616 (2017).

[86] K. Ueno and K. Fukushima, Changes in structure and chemical composition of α-$MoTe_2$ and β-$MoTe_2$ during heating in vacuum conditions, Appl. Phys. Express **8**, 095201 (2015).

[87] K. Zhang, C. Bao, Q. Gu, X. Ren, H. Zhang, K. Deng, Y. Wu, Y. Li, J. Feng, and S. Zhou, Raman signatures of inversion symmetry breaking and structural phase transition in type-II Weyl semimetal $MoTe_2$, Nat. Commun. **7**, 13552 (2016).

[88] T. Boöker, R. Severin, A. Müller, C. Janowitz, R. Manzke, D. Voß, P. Krüger, A. Mazur, and J. Pollmann, Band structure of MoS_2, $MoSe_2$, and $MoTe_2$: Angle-resolved photoelectron spectroscopy and *ab initio* calculations, Phys. Rev. B **64**, 235305 (2001).

[89] S. Tang, C. Zhang, C. Jia, H. Ryu, C. Hwang, M. Hashimoto, D. Lu, Z. Liu, T. P. Devereaux, Z. X. Shen, and S. K. Mo, Electronic structure of monolayer 1T′-$MoTe_2$ grown by molecular beam epitaxy, APL Mater. **6**, 026601 (2018).